The inner junction complex of the cilia is an interaction hub that involves tubulin post-translational modifications.

Ahmad Khalifa[1,4§], Muneyoshi Ichikawa[1§†], Daniel Dai[1,4], Corbin Black[1,4], Katya Peri[1], Thomas S. McAlear[1,4], Shintaroh Kubo[3,4], Simon Veyron[2,4], Shun Kai Yang[1,4], Javier Vargas[1,4], Jean-Francois Trempe[2,4], Susanne Bechstedt[1,4], Khanh Huy Bui[1,4*]

[1]Department of Anatomy and Cell Biology, McGill University, Montréal, Québec, Canada, H3A 0C7

[2]Department of Pharmacology, McGill University, Montréal, Québec, Canada, H3A 0C7

[3]Department of Biophysics, Graduate School of Science, Kyoto University, Kyoto 606-8502, Japan

[4]Centre de Recherche en Biologie Structurale - FRQS, McGill University, Montreal, Quebec, Canada

[§] These researchers contributed equally to this work

[†]Present address: Department of Systems Biology, Graduate School of Biological Sciences, Nara Institute of Science and Technology, 8916-5, Takayama-cho, Ikoma, Nara 630-0192, Japan

[*] **Corresponding author. E-mail:** huy.bui@mcgill.ca

Short: Inner junction complex of the cilia

Keywords: microtubule, cilia, axoneme, cryo-electron microscopy, acetylation, inner junction

Abstract

Microtubules are cytoskeletal structures involved in structural support, microtubule-based transport and the organization of organelles in the cells. The building blocks of the microtubule, the α- and β-tubulin heterodimers, polymerize into protofilaments, that associate latterly to form the hollow microtubule. There exists a specific type of microtubule structures, termed doublet microtubules, in the cilia where high stability is required for ciliary beating and function. The doublet microtubule consists of a complete A-tubule and a partial B-tubule. The doublet microtubule maintains its stability through the binding of microtubule inner proteins in the lumen of the A- and B-tubules and via unique interactions at its outer and inner junctions, where the A- and B-tubules meet.

Here, we present the answer to the long-standing question regarding the identity, localization and structure of the inner junction proteins in *Chlamydomonas* doublet microtubules. We show that inner junction proteins PACRG and FAP20, together with FAP52, previously unidentified FAP276 and an unknown Tether protein, form an interaction hub at the inner junction, which involves tubulin sites for post-translational modifications. We further compare the *Chlamydomonas* and *Tetrahymena* doublet microtubule structures to understand the common and species-specific features of the inner junction.

INTRODUCTION

Cilia and flagella are highly conserved organelles present in protists all the way to humans. They are commonly classified into two forms: motile and non-motile cilia. Motile cilia are responsible for mucus clearance in the airway, cerebrospinal fluid circulation and sperm motility (1). The non-motile cilia, namely primary cilia, function as the cellular antennas that sense chemical and mechanical changes. Cilia are essential for growth and development and therefore human health. Defects in cilia often result in abnormal motility or stability, which lead to cilia-related diseases such as primary ciliary dyskinesia, retinal degeneration, hydrocephalus and polydactyly (2).

Both cilia types are comprised of a bundle of nine specialized microtubule structures termed doublet microtubules (doublets). Ciliary components, important for motility such as the outer and inner dynein arms, radial spokes and the dynein regulatory complex (DRC) are assembled onto the surface of the doublet (3-6). Inside the doublets, is a weaving network of proteins, termed microtubule-inner-proteins (MIPs), that bind to the inner lumen surface of the doublet (7, 8). These MIPs act to stabilize the microtubule and very likely regulate the ciliary waveform through interactions with the tubulin lattice (8).

Doublets consists of a complete 13-protofilament (PF) A-tubule, similar to a 13-PF cytoplasmic microtubule and a partial 10-PF B-tubule forming on top of the A-tubule. To this day there still exists a long-standing question of how the junctions between the two tubules are formed (9-11). Recent high-resolution cryo-EM structure of the doublet shows that the outer junction is formed by a non-canonical tubulin interaction between PF B1 and PF A10 and A11 (7). The inner junction (IJ), which bridges the inner gap between the B-tubule and A-tubule is formed by non-tubulin proteins. Both primary and motile cilia have been observed to contain the IJ (11, 12).

In vitro formation of a B-tubule-like hook (i.e. the outer junction like interaction) was assembled onto pre-existing axonemal and mitotic spindle microtubule with the addition of purified brain tubulin (13). More recently, the B-tubule-like hook can be achieved by adding purified tubulins onto existing subtilisin treated microtubule (14). However, these hooks are not closed and appear to be very flexible (14). This supports the notion that the IJ is composed of non-tubulin proteins that are indispensable to the stability of the IJ.

The IJ is composed of FAP20 as shown through cryo-electron tomography and BCCP-tagging (15). Dymek et al (16) reported that PArkin Co-Regulated Gene (PACRG) and FAP20 proteins form the IJ. PACRG and FAP20 are arranged in an alternating pattern to form the IJ linking the A- and B-tubule protofilaments A1 and B10 of the axonemal doublets. In addition, both FAP20

and PACRG are important components for motility. Both PACRG and FAP20 are conserved among organisms with cilia, suggesting a common IJ between species.

PACRG, as the name suggests, is co-regulated with the Parkinson's disease-related gene parkin (17, 18). Due to its axonemal functions, knockdown of PACRG genes in *Trypanosoma brucei* and *Xenopus*, lead to defects in the doublet structure and, therefore, impaired flagellar motility. In vertebrates, defects in left-right body symmetry, neural tube closure were observed from knockdowns of PACRG (19). In mice, PACRG knockout results in male sterility (20) and hydrocephalus (21). FAP20 knockout mutants in *Chlamydomonas* have motility defects and frequent splaying of the axoneme (15). Similarly, FAP20 knockdown in *Paramecium* has an altered waveform (22). A recent report identified other MIPs near the IJ, namely FAP52 and FAP45 (23). Knockouts of FAP52 or FAP45 lead to an unstable B-tubule. Double knockouts of FAP52 or FAP45 together with FAP20 leads to severe damage of the B-tubule. The gene deletion of the human homolog of FAP52 has been shown to cause heterotaxy and *situs inversus totalis* in patients (24).

Cryo-EM structures of isolated doublets from *Tetrahymena* show that there are different tethering densities that connect the B-tubule to the A-tubule aside from the IJ (7, 8). Taken together, these data suggest that there is a complex interaction at the IJ region involving multiple proteins in addition to PACRG, FAP20, FAP45 and FAP52. These interactions may play a role in regulating ciliary motility via stability.

Despite all the phenotypes known about these IJ proteins, there are no high-resolution structures to explain the molecular mechanism of the B-tubule closure and IJ stability. In this study, we present the high-resolution cryo-EM structure of the inner junction region from the *Chlamydomonas* doublet. We also compare the *Chlamydomonas* structure with the *Tetrahymena* structure to understand the common and species-specific features of the IJ. We also report the identity of a new IJ protein: FAP276. Our results suggest that the IJ is made up of a complex of proteins involving PACRG, FAP20, FAP52, FAP276 and other unknown proteins that exist in their environment.

RESULTS

Multiple tether proteins exist at the IJ

To better understand the IJ, we obtained the 48-nm repeating unit of taxol stabilized and salt treated *Chlamydomonas* doublet at 4.5 Å resolution (Fig. 1A-B and Fig. S1A-C). Due to the salt wash, some MIPs were lost when compared to the intact tomographic doublet structure (dashed parts in Fig. 1B) (5). When comparing to the cryo-EM structure of the 48-nm repeating

unit of *Tetrahymena* (7, 8), the IJ region bridging PF B10 and A1 remained intact (Figure 1A-D). Based on previous studies (15, 16, 23), we were able to localize FAP52, FAP45 in both *Tetrahymena* and *Chlamydomonas* (FAP52, light green and FAP45, yellow-green in Fig. 1E, G), and PACRG and FAP20 (PACRG, light gray and FAP20, dark gray in Fig. 1F) in *Chlamydomonas*.

In this study, we termed the structure formed by the repeating units of PACRG and FAP20, the IJ protofilament (IJ PF), and refer to the IJ complex as all the proteins involved in the attachment of the B-tubule to the A-tubule. Most of the proteins in this IJ complex are attached to PFs B8 to B10 and the IJ PF.

The presence of the IJ PF stabilizes the B-tubule of the *Chlamydomonas* doublet relative to *Tetrahymena*, as evidenced by local resolution measurements (Fig. S1D). Despite having a good resolution in the A-tubule, the *Tetrahymena* doublet has a poorer resolution in the IJ area of the B-tubule.

Inside the B-tubule of both species, it is clear that the IJ region is held up by many tether densities along the doublet connecting the B-tubule to PF A13 (Fig. 1E-G). First, the B-tubule is held up by tether density 1 (red, Fig. 1H), referred to as MIP3b previously (7, 8). Tether density 1 connects the PF B9/B10 and A13. The second connection is named Tether density 2 (red, Fig 1E-G), projecting from the proximal lobe of the FAP52 density (referred to as MIP3a previously (7)) and connecting to PF A13 (Fig. 1H). In *Chlamydomonas*, there is another Y-shaped density (purple) cradling the FAP52 proximal lobe density and projects into the gap between the IJ PF and PF B10 (Fig. 1H).

FAP45, which is referred to as MIP3c previously (23) is a filamentous MIP binding at the inner ridge between PF B7 and B8. In both species, FAP45 forms an L-shape density which contacts FAP52 once every 48-nm. This explains the zero-length cross-link observed in a recent study (23). In *Tetrahymena*, there exists a tether density 3 (pale violet, Fig. 1), projecting from the distal lobe of the FAP52 density and connecting to PF A13. This Tether density 3 is not present in the *Chlamydomonas* doublet, suggesting that this density is specific to Tetrahymena. All the tether densities described above repeat with 16-nm.

The IJ PF is formed by a heterodimer of PACRG and FAP20 repeating every 8-nm with the same repeating unit as tubulin dimers (Fig. 1F). This is not surprising because the purpose of the IJ PF is to bridge the tubulin dimers from PFs B10 and A1. In the 48-nm *Chlamydomonas* doublet map, there is one PACRG unit with a less defined density compared to the others (dashed box, Fig. 1F). It has been shown that there is one PACRG density missing in every 96-nm repeat (6, 16). Since our doublet map is a 48-nm repeat unit, the less defined density of PACRG

corresponds to the average from one unit of PACRG and one missing unit. This missing unit of PACRG in the 96-nm repeat allows the basal region of the DRC to anchor onto the doublet (6) (Fig. S1F, G).

The entire IJ filament of PACRG and FAP20 seems to be missing in the *Tetrahymena* structure. Upon adjusting the threshold value of the surface rendering, we observed one dimer of PACRG and FAP20 remaining in the structure, previously named the inner junction small structure (Fig. S1E) (7). This can be a result of a specific region every 96-nm of the *Tetrahymena* doublet that can hold this dimer in place but not washed away during the preparation.

We reasoned that since FAP52 interacts with a few proteins in the IJ complex, knockout of FAP52 might lead to reduction of those proteins. Therefore, we performed mass spectrometry of FAP52 mutant from *Chlamydomonas* and performed relative quantification of axonemal proteins compared to wild type (Supplementary Table 1). We observed 12 missing and 26 proteins reduced by at least 2-fold. PACRG, FAP20 and FAP45 levels are unchanged in FAP52 mutants since there level of interaction with FAP52 are quite small as supported by our structure. The level of tektin, another suggested IJ protein does not change as well.

PACRG, FAP20, FAP52 and FAP276 form an IJ complex

Since the majority of IJ proteins repeat with 8-nm and 16-nm, we obtained the focused refined maps of the IJ complex with a 16-nm repeating unit from *Chlamydomonas* and *Tetrahymena* at 3.6 Å resolution (Fig 2A-B and Fig. S1C). Without the IJ PF, the B-tubule is flexible in *Tetrahymena*, which leads to less resolution in the IJ area despite the 3.6 Å resolution in the A-tubule. In contrast, the IJ region of *Chlamydomonas* has good resolution due to the stability of the B-tubule as a result of the intact IJ PF. Therefore, we were able to de novo model PACRG, FAP20 and FAP52 in *Chlamydomonas* (Fig. 2A, B and Fig. S2A-F). We could not model FAP45 since FAP45 repeats with 48-nm, and therefore is averaged out in the 16-nm averaged map.

We were also able to trace and estimate the molecular weight of the Y-shaped density to ~85 amino acids and ~10 kDa. Since this density is repeating with 16-nm and has a large binding interface with FAP52, we hypothesized that this protein would be missing in a FAP52 mutant. From the FAP52 knockout mass spectrometry data, FAP276 fit our search criteria and was completely missing when compared to the wild type mass spectrometry. Both the secondary structure prediction and the sequence of FAP276 unambiguously agree with the density signature in this region. Therefore, the inner junction is made up of an 8-nm repeat of PACRG and FAP20 and a 16-nm repeat of FAP52 and FAP276 (Fig. S2I).

The PACRG structure is composed mainly of α-helices with a long unstructured N-terminal region. PACRG contains an alpha solenoid architecture, similar to the microtubule binding TOG domain, which is present in many microtubule polymerases (25, 26). The N-terminal region extends over PF A1, goes inside the outside wedge between PFs A1 and A13 and folds back to form a stable triple helix arrangement with the core of the protein (Fig. 2H, S2A).

On the other hand, FAP20 consists of mainly β-sheets with a small helix. According to the CATH protein structure classification database, FAP20 has a beta jelly rolls architecture, which is normally observed in carbohydrate binding modules and viral capsids (27). The C-terminus of FAP20 is located at the outside of the doublet, in agreement with a tomographic study of FAP20 with a Biotin Carboxyl Carrier Protein tag at the C-terminus. (15).

PACRG binds to the inter-dimer interface of PF B10 and mainly β-tubulin from PF A1. FAP20 is sandwiched by the tubulin dimer from PF B10 and the α-tubulin from PF A1 (Fig. 2C). PACRG and FAP20 have two microtubule-binding sites, one on the surface of the A-tubule similar to well-studied microtubule-associated protein binding sites such as TOG (26), and one on the lateral side of the B-tubule (Fig. 2D). The lateral binding site is unique and has never been observed in previously known microtubule-associated proteins.

Both PACRG and FAP20's interactions with tubulin from PF A1 appear to be electrostatic. The outside surface of α- and β-tubulin is highly negatively charged while the corresponding interacting surfaces of tubulin are positively charged (Fig. 2E). Despite the fact that PACRG contains alpha solenoid architecture like TOG domains, the binding orientation of PACRG to the surface of tubulin is completely different from TOG domain binding (26).

In our structure, we also observe that the distance between FAP20 and the proximal PACRG is closer compared to the distal PACRG, thus they likely form and assemble as heterodimers (Fig. S2J). The PACRG and FAP20 binding interface appears to involve multiple hydrogen bonds with complementary surface charges, suggesting a specific and strong interaction. (Fig. S2K, L).

In addition to the interactions highlighted above, we also observed the interaction of the β-tubulin C-terminus from PF A1 with PACRG (Fig 2F, G). The C-terminus of α- and β-tubulin are a hot spot for post-translational modifications such as polyglutamylation and polyglycylation (28). However, due to its flexibility, densities for the α- and β-tubulin C-termini are usually not visible in microtubule cryo-EM reconstructions. This is also the case for the outside of the A- and B-tubules in our *ex vivo* structure. However, in the lumen of the B-tubule, the β-tubulin C-terminus from PF A1 appears to be stabilized by two key interactions with PACRG: the hydrogen

bond between D432 together with the hydrophobic burial and the stable T-shaped stacking of F436 with N251 and Y249 of PACRG, respectively (Fig. 2G). Both interactions stabilize the β-tubulin C-terminus forming a helical turn in segment E432-E437, which otherwise wouldn't be present due to its flexibility.

This structuring of the β-tubulin C-terminus in PF A1 appears to be the result of the steric proximity with the PACRG's N-terminus. Thus, both interactions are important in maintaining the stability of the inner junction by preventing steric clashing between the two. It could also be an indication of further post-translational modifications that occur in this region, which could have a potential role in inner junction formation and stability.

The cryo-EM structure of the *Chlamydomonas* PACRG is highly similar to the crystal structure of the human PACRG binding to MEIG1 (PDB: 6NDU), suggesting a conserved role of PACRG. However, *Chlamydomonas* PACRG has a long N-terminus that binds on top of PF A13 and into the wedge between PF A1 and A13 (Fig. 2H, Fig. S2A). This N-terminal region is not conserved in human or *Tetrahymena* and is either truncated or not visible in the crystal structure of human PACRG. This could indicate organism-specific adaptations to achieve finely tuned degrees of ciliary stability.

FAP52 forms an interaction hub and stabilizes α-tubulin's acetylation loop

Next, we investigated the structure of FAP52 (Fig. S2C). FAP52 consists of eight WD40 domains forming two seven-bladed beta-propellers. The two beta-propellers form a V-shape that docks onto PF B10 and B9. The proximal beta-propeller docks onto the inside of the α- and β-tubulin intra-dimer interface, while the distal beta-propeller is aligned with the next inter-dimer interface towards the plus end (Fig. 3A).

The distal beta-propeller of FAP52 has a 3-point contact with the inner surface of the B-tubule (Fig. 3B, C). Two of the FAP52 contacts involve the K40 loop of α-tubulin from PF B9 and B10. This K40 loop has not been fully visualized in reconstituted studies of acetylated tubulins. In our structure, the K40 loop is fully structured and visualized in this position (Fig. 3D, E and Fig. S3D-G). For the first contact point, residue R225 of FAP52 seems to interact with D39 of α-tubulin from PF B10 (Fig. 3F, G). At the second tubulin contact point, FAP52 segment G142-P143 appears to interact with T41 of α-tubulin from PF B9. The third contact involve Q293 with T35 and T192-R195 with S78 at the interface between FAP52's distal beta propeller and β-tubulin, respectively (data not shown). In the lower region of FAP52, residue N275 from the distal beta-propeller's V268-L279 loop appears to interact with segment P25-A27 of the N-terminus of PACRG (Fig. 3G).

In contrast to the *Tetrahymena* doublet (Fig. S3A, B), the density of the aforementioned loop is not present in the FAP52 structure. Apparently, this long loop (V268 to L279) is in fact, deleted in other species (Fig. S3C). The interaction of this loop with *Chlamydomonas* PACRG suggests that it is a *Chlamydomonas* specific feature that stabilizes PACRG and, hence the IJ PF.

We then investigated all the K40 loops from *Chlamydomonas* and *Tetrahymena* doublets (Fig. S3D-G). When there is no interacting protein, this loop is flexible consistent with previous literature (29). However, we were able visualize the loop in several places in both *Chlamydomonas* and *Tetrahymena* where there is an interacting protein (Fig. S3F, G). The conformation of the loop appeared to differ depending on the identify and orientation of its interacting protein. This suggests that the α-K40 loop could have a role in MIP recognition and binding.

Furthermore, because of the V-shape of FAP52, its contact with tubulin is minimal. The existence of a cradling protein such as FAP276 then makes sense from a functional standpoint since it appears to support and mediate FAP52's interactions with tubulin (Fig. 4H). Segment L52-H57 from FAP276 forms beta sheet-like stacking interactions with segment L375-V380 from FAP52 (Fig. 4H, I). FAP276 itself forms numerous interactions with tubulin with both of its N- and C-termini, thus it provides strong anchorage for FAP52 to the tubulin lattice (Fig 4H-K). Given FAP52's numerous interactions with all the proteins mentioned, it is likely to function as an interaction hub, which could play a role during IJ assembly.

Tether density 1 and 2 form the Tether loop

We were able to trace the densities related to the Tether structures in the 16-nm averaged map. Tether density 1 is connected to Tether density 2 (Fig. 4A-D), forming a Tether loop, through which the A- and B-tubules are connected. The loop connecting the Tether density 1 binds on top of PF A12 and then into the outside wedge between A12 and A13 before connecting with Tether density 2. This Tether loop density is conserved between *Tetrahymena* and *Chlamydomona*s. It is likely that the entire Tether loop is composed of a single polypeptide. In addition, the loop seems to resemble Tau binding to the microtubule (30). There is a small helical region in this loop that binds to α-tubulin of PF A12 (Fig 4G and Fig. S4G).

We also observed in *Chlamydomonas* another density, we termed the hook density, binding on PF A13 and also in the wedge between PF A12 and A13. This density is part of MIP5 described previously (Fig. S4B) (7). This density shows no secondary structure pattern and can be traced as a single polypeptide. Almost half of this density seems to run along the wedge between PF A12 and A13, close to the tubulin lateral interface. The protein corresponding to this density might act as a low curvature inducer from the outside similar to Rib43a from the inside (Fig. S4C).

In *Tetrahymena*, in place of the hook density, the surface of PF A12 is bound by Tether density 3. Tether density 3 connects the distal lobe of FAP52 and binds across the wedge between PF A13 and A1. (Fig. 4H). Upon superimposing the *Chlamydomonas* PACRG structure onto the *Tetrahymena* IJ area, we observed that the N-terminus of PACRG will have a steric clash with Tether density 3 (Fig. 4I). Therefore, the N-terminus of *Tetrahymena* PACRG might bind differently or only bind to PF A1. This is supported by the shorter N-terminus of *Tetrahymena* PACRG relative to the *Chlamydomonas* PACRG Sequence. Tether density 3 might interact with and perform the same function as the N-terminus of PACRG in *Chlamydomonas*, which induces high curvature of PF A13 and A1.

DISCUSSION

In this study, we describe the molecular details of the IJ. The IJ is a complex made up of PACRG, FAP20, FAP52, FAP276, FAP45 and their intricate interactions. In both *Chlamydomonas* and *Tetrahymena*, this complex is further complicated by other unidentified densities such as the Tether densities. We identified a new member of the IJ, FAP276, which is *Chlamydomonas*-specific. FAP276 forms strong beta sheet-like interactions with FAP52 as well as tubulin from PF B9 and B10. FAP52, FAP276 and the Tether loop anchor the B-tubule to the A-tubule while the IJ PF, composed of PACRG and FAP20, closes the IJ gap. For the doublet to withstand the mechanical strain during ciliary beating, it needs all the anchoring points for proper stability. Tektin, a coiled-coil protein, was also proposed to be another component of the IJ complex in *Chlamydomonas* by biochemical experiments (15). However, no filamentous density corresponding to tektin was found at the IJ PF in our *Chlamydomonas* map.

As previously reported, our *Tetrahymena* doublet structure lacked the IJ PF (7, 8). Our IJ PF from *Chlamydomonas* fits in the gap between PF A1 and B10 in the *Tetrahymena* doublet without clashing. Since PACRG and FAP20 homologues are present in the *Tetrahymena* doublet (Ichikawa, Liu et al. 2017), the missing IJ PF could be attributed to the sample preparation of the doublet as well as the structural differences between the two doublets. Reconstituted doublet microtubules (14) indicate that the B-tubule cannot be closed and is extremely flexible without the IJ PF. Therefore, the IJ PF is necessary to dock the B-tubule onto the A-tubule. In *Tetrahymena*, even with the presence of FAP52 and the Tether loop, the doublet is still flexible which can be seen by the lower resolution of the B-tubule compared to the A-tubule (Fig. S1D). In addition, the B-tubule can be subjected to depolymerization when the IJ PF is not fully formed (23). Therefore, the IJ PF serves as an anchor, which protects the B-tubule from depolymerization by shielding the lateral side of PF B10 (Fig. 5). Because of the complexity of interactions and the diverse protein composition of the IJ complex, it is reasonable to assume that the IJ is assembled after the outer junction nucleates and expands towards the IJ. The IJ

complex might be assembled or co-assembled at the same time as PF B10 for the closure of the B-tubule (Fig. 5).

When comparing *Chlamydomonas* and *Tetrahymena* doublets, the IJ complex seems to contain many conserved components such as the Tether loop, PACRG, FAP20, FAP52 and FAP45. There are also species-specific proteins such as FAP276 and the hook density in *Chlamydomonas* and Tether density 3 in *Tetrahymena*. Interestingly, Tether density 3 clashes with a superimposed *Chlamydomonas* FAP276 structure, suggesting that it takes over its role in mediating the interactions between FAP52 and tubulin in *Tetrahymena*. This suggests that there is a common framework for the IJ complex in all doublets. Species-specific proteins may then fine-tune this framework according to its survival needs.

Furthermore, our atomic models could explain the severe motility phenotypes observed in PACRG and FAP20 mutants compared to FAP52 mutant. Mutants in either PACRG or FAP20 might affect the stability of the DRC, which can severely affect the regulation of ciliary beating. This is supported by the fact that FAP20 mutant is prone to splaying of the cilia (15). Our results could also explain how the double knockout of FAP20 along with FAP45 or FAP52 can affect B-tubule stability at the IJ (23). In such conditions, both the IJ PF and the FAP52 or FAP52-mediated anchorage between the A- and B-tubules will be completely lost.

This is further supported by the atomic models of PACRG and FAP20 which illustrate their binding interfaces with the doublet. Both the surface interactions of PACRG and FAP20 with the A-tubule involve electrostatic interactions, in a similar fashion to many microtubule-associated proteins (26). As for the B-tubule interface, PACRG appears to form numerous interactions with the lateral side of tubulin, suggesting an important role in B-tubule closure (Fig. 2D), while FAP20 seems to have minimal to no contact with the lateral side. Recent work shows that human PACRG-MEIG1 complex can prevent tubulin sheet closure, supporting the lateral interaction of PACRG (31). This infers that the transport of FAP20 and PACRG to the right position during assembly must be regulated.

During doublet assembly, if PACRG and FAP20 bind to the B-tubule lateral interface before PF B10 assembly, it would lead to an incomplete B-tubule. To facilitate a successful IJ assembly, chaperones might be needed for the transport of PACRG and FAP20. PACRG forms a complex with MEIG1 (31). Even though MEIG1 is not present in lower eukaryotes and that the MEIG1 binding loop is not conserved between *Chlamydomonas* and humans, a chaperone similar to MEIG1 can function to target PACRG to the lateral interface of the PF B10.

Our atomic models support that PACRG and FAP20 might form a heterodimer before their transport and assembly into the cilia (Fig. S2J). Surprisingly, FAP20 shows a similar fold and mode of binding to a class of proteins called carbohydrate binding modules. Carbohydrate

binding modules form a complex with carbohydrate-active enzymes and are known to have a substrate targeting and enzyme-concentrating function (32). This supports a role of FAP20 as an assembly chaperone in a FAP20-PACRG complex. Furthermore, both studies from Yanagisawa et al. (15) and Dymek et al. (16) show reduced endogenous PACRG in *Chlamydomonas* FAP20 knockout mutant. In the latter study, it was shown that the assembly of exogenous PACRG was less efficient in the FAP20 knockout compared to conditions where FAP20 was intact. This implies that PACRG assembly might indeed depend on FAP20 (15).

The numerous N-terminus contacts of *Chlamydomonas* PACRG with both tubulin and the unique FAP52 loop in *Chlamydomonas* could explain the *Chlamydomonas* IJ stability following sample preparation. The N-terminus of *Chlamydomonas* PACRG penetrates the wedge between PF A13 and A1 and forces the PF pairs into a high-curvature conformation (Fig. S4C). As it can be seen from the curvature analysis, PF A13 and A1 have a sharp curvature change from PF A11 and A13. Alternatively, the curvature might be enforced by MIPs inside the A-tubule. The N-terminus of PACRG might act as the curvature sensor for the specific binding and anchoring of PACRG to the right position. It has been shown that doublecortin can sense the curvature of 13-PF microtubule (33). Since the length of the N-terminus of PACRG is generally not conserved, it is likely that the shorter PACRG N-terminus in *Tetrahymena* does not bind strongly to the doublet and therefore, detaches during sample preparation. In *Tetrahymena*, Tether density 3, which is not present in *Chlamydomonas* seems to be a high curvature inducer and IJ complex stabilizer.

POC16 is a homolog of FAP20 that exists In the *Chlamydomonas* centriole (Hamel, Steib et al. 2017). In contrast to FAP20, POC16 is a much larger protein, containing a FAP20 domain followed by several WD40 domains. Therefore, POC16 might function as a fusion protein of FAP20 and FAP52 carrying out the function of both. This may improve the stability of the IJ region in the centriole. In higher eukaryotes, there exists PACRG and PACRG-like proteins in the centriole and axoneme. The PACRG-like proteins normally lack the N-terminal regions compared to PACRG. This suggests that the N-terminus of PACRG proteins are important for specific functions.

Post-translational modifications in tubulin are known to be important for the activity of the cilia. The α-K40 acetylation was first discovered in *Chlamydomonas* flagella, which is almost fully acetylated (34). In 3T3 cells, the K40 acetyltransferase, αTAT1 promotes rapid ciliogenesis (35). However, it is still not clear what the direct effect of K40 acetylation is.

Since then, there have been many studies about the effect of acetylation on the properties of microtubule such as stability (36, 37). A recent cryo-EM study of reconstituted acetylated microtubules showed, using molecular dynamics, that the acetylated α-K40 loop has less conformational flexibility, but a full α-K40 loop in the cryo-EM map has not been visualized due

to its flexibility. In this work, we show that the acetylated K40 loop binds to FAP52 and forms a fully structured loop. This loop remains flexible and unstructured when there is no interacting protein. This suggests that the α-K40 loop has a role in protein recruitment and interactions, especially, MIPs. We hypothesize that the acetylation disrupts the formation of an intra-molecular salt bridge between K40 and D39, which affects the loop's sampling conformations and allows D39 to take part in atomic interactions with other proteins. This, in turn, improves the stability of the doublet and therefore, correlates with axonemal motility. The absence of acetylating enzymes has indeed been shown to affect sperm motility in mice (38). while SIRT2 deacetylation decreases axonemal motility in vitro (39).

In neurons, microtubules are also highly acetylated and are known to be stable. Our hypothesis suggests that in neuron microtubules, MIPs might have a similar stabilizing effect as in the doublet. Previous studies on olfactory neurons demonstrate that there are densities of proteins inside the microtubule, suggesting the existence of MIPs inside cytoplasmic microtubules (40).

Another interesting insight from our study is the structured C-terminus of β-tubulin. The C-termini of tubulin in the doublet normally have polyglycylation and polyglutamylation, in particular, the B-tubule (41). In reconstituted microtubules and other places in the doublet, the C-termini are highly flexible and cannot be visualized. However, we observed the C-terminus of β-tubulin in PF A1 which appears to interact with PACRG and FAP20. This suggests that the C-terminus might have a role in the assembly and or stability of the doublet.

Defects in tubulin polyglutamylase enzyme have indeed led to partially formed B-tubules (42). This could indicate a role for polyglutamylation in the interaction and recruitment at the IJ PF, specifically PACRG and FAP20. Lack of polyglutamylation can lead to an easily detachable PACRG and FAP20 and hence the partial assembly of the B-tubule. Finally, it is possible that MIPs can act as sensors for the post-translational modifications of tubulin for their orderly recruitment and assembly.

MATERIALS AND METHODS

Preparation of doublet samples

WT Chlamydomonas cells (cc124) were obtained from *Chlamydomonas* source center and cultured either on Tris-acetatephosphate (TAP) media with shaking or stirring with 12 hr light-12 hr dark cycle. For flagella purification, *Chlamydomonas* cells were cultured in 1.5 L of liquid TAP media with stirring until OD600 reached around 0.5-0.6 and harvested by low-speed centrifugation (700g for 7 min at 4°C). *Chlamydomonas* flagella were purified by dibucaine method (43), resuspended in HMDEKP buffer (30 mM HEPES, pH 7.4, 5 mM MgSO4, 1 mM DTT, 0.5 mMc, 25 mM Potassium Acetate, 0.5% polyethylene glycol, MW 20,000) containing 10 µM paclitaxel, 1 mM PMSF, 10 µg/ml aprotinin and 5 µg/ml leupeptin. Paclitaxel was added to the buffer since *Chlamydomonas* doublets were more vulnerable to high salt extraction compared with *Tetrahymena* doublets (data not shown). Isolated flagella were demembraned by incubating with HMDEKP buffer containing final 1.5% NP40 for 30 min on ice. After NP40 treatment, *Chlamydomonas* doublets were incubated with final 1 mM ADP for 10 min at room temperature to activate dynein and then incubated with 0.1 mM ATP for 10 min at room temperature to induce doublet sliding. Since the *Chlamydomonas* doublets were harder to split compared to *Tetrahymena* doublet, sonication was done before ADP/ATP treatment. After this, *Chlamydomonas* doublets were incubated twice with HMDEKP buffer containing 0.6 M NaCl for 30 min on ice, spinned down (16,000 g and 10 minutes), and resuspended. *Chlamydomonas* doublets were not dialyzed against low salt buffer since it was difficult to remove radial spokes. The gel of purification process is in Supplementary Fig. 1A.

Tetrahymena doublets were isolated according to our previous work (7, 8).

Cryo-electron microscopy

3.5 ul of sample of doublets (~4 mg/ml) was applied to a glow-discharged holey carbon grid (Quantifoil R2/2), blotted and plunged into liquid ethane using Vitrobot Mark IV (Thermo Fisher Scientific) at 25°C and 100% humidity with a blot force 3 or 4 and a blot time of 5 sec.

9,528 movies were obtained on a Titan Krios (Thermo Fisher Scientific) equipped with Falcon II camera at 59,000 nominal magnification. The pixel size was 1.375 Å/pixel. Dataset for *Tetrahymena* was described in Ichikawa et al. (8). *Chlamydomonas* dataset was collected with a dose of 28-45 electron/Å2 with 7 frames. The defocus range was set to between -1.2 and -3.8 um.

The Chlamydomonas doublet structures were performed according to Ichikawa et al. (8). In short, movies were motion corrected using MotionCor2 (44). The contrast transfer function were estimated Gctf (45). The doublets were picked using e2helixboxer (46).

270,713 and 122,997 particles were used for the 16-nm reconstruction of 48-nm repeating unit of *Chlamydomonas*. 279,850 particles were used for the 16-nm reconstruction of *Tetrahymena*. The final Gold Standard FSC resolutions of the 16-nm and 48-nm reconstruction for Chlamydomonas after contrast transfer function refinement and polishing using 0.143 FSC criterion in Relion3 (47) are 4.5 and 3.8 Å, respectively. Using focus refinement of the IJ of the 16-nm reconstruction for Chlamydomonas, the resolution reaches 3.6 Å resolution. The resolution for the 16-nm reconstruction of Tetrahymena was 3.6 Å. Focus refinement of the IJ of Tetrahymena did not improve the resolution of the IJ due to the flexibility of this region. The maps were local sharpened (8). Local resolution estimation was performed using MonoRes (48).

Modelling

C. reinhardtii α-β-tubulin

A homology model of *C. reinhardtii* α-β-tubulin (Uniprot sequence α: P09204, β: P04690) was constructed in Modeller v9.19 (49) using PDB 5SYF as template. The model was refined using real-space refinement (50) and validated using comprehensive validation for cryo-EM in Phenix v1.16 (51).

PACRG and FAP20

A partial homology model of *C. reinhardtii* PACRG (B1B601) was constructed using the crystal structure of the human homolog (Q96M98-1) as template (31). The model was completed by building segments N2-D148 and Y249-L270 *de novo* in density using Coot v0.8.9.1 (52). The density for segment M89-K101 is missing, likely due to flexibility in this region. *C. reinhardtii* FAP20 (A8IU92) was completely built *de novo* in density. Both models were refined and validated as described for α-β-tubulin.

FAP52

The density was traced in Coot v0.8.9.1 (52) according to a double beta-propeller topology similar to PDB 2YMU, which agrees with the I-TASSER (53) tertiary structure prediction of FAP52 (Uniprot: A0A2K3D260). The bulky residues of FAP52 were used as anchors to maintain the correct registry in lower resolution areas. The model has been overfit on the left side (segment D341-P627) where the density signal is significantly lower, likely due to heterogeneity. The final model was refined and validated as described above.

FAP276

The density for FAP276 was segmented and traced to around 80 amino acids and ~9 KD in mass. Candidates from the wild type mass spectrometry data were compared to the FAP52 knockout data and reduced to only FAP276, which was completely missing the latter. The secondary structure prediction (54) as well as the sequence of FAP276 (Phytozome: Cre04.g216250) agree unambiguously with the density signature in that region. The model was traced, refined and validated as described above.

Inter-PF angle (lateral curvature) measurement

The inter-PF angle between each PF pair are measured according to Ichikawa *et al*., (7).

Visualization

The maps and models were segmented, coloured and visualized using Chimera (55) and ChimeraX (56).

Mass spectrometry

Sample preparation and mass spectrometry of FAP52 mutant and relative quantification compared to wild type *Chlamydomonas* was done according to Dai et al., 2019. (57).

ACKNOWLEDGEMENT

We acknowledge the Facility for Electron Microscopy Research of McGill University, in particular Drs. Kaustuv Basu and Kelly Sears where our cryo-EM experiments were conducted. This research was supported by funding from the Natural Sciences and Engineering Research Council of Canada (RGPIN-2016-04954), Canada Institute of Health Research (CIHR PJT-156354), the Canada Institute for Advanced Research Arzieli Global Scholars Program (to K.H.B.). M.I. is supported by Japan Society for the Promotion of Science Overseas Research Fellowships. A.A.Z.K. is supported by CIHR and the Al Ghurair Foundation for Education. S.K. is supported by a JSPS Overseas Challenge Program for Young Researchers. We declare no competing financial interests.

FIGURE CAPTION

Figure 1: The IJ structures of *Chlamydomonas* and *Tetrahymena* doublet.

(A-D) Surface renderings and schematics of the 48-nm repeat cryo-EM maps of *Chlamydomonas* (A, B) and *Tetrahymena* (C, D) doublets viewed from the tip of the cilia. Black arrow indicates longitudinal view in (E), (F) and (G). (E-F) The longitudinal section of the *Chlamydomonas* doublet at the IJ complex from the inside (E) and outside (F). (G) The longitudinal section of *Tetrahymena* doublet viewed from the inside. Color scheme: FAP20: dark gray; PACRG: gray; FAP52: light green, Y-shaped density: purple; FAP45: yellow green; fMIP-B8B9: orange; Tubulin: light gray; Rest of MIPs: white; Tether density 1 and 2: red; Tether density 3, pink. Plus and minus ends are indicated by + and - signs. (H) Cross sectional views of the different Tether densities from *Chlamydomonas* (left) and *Tetrahymena* (right). In *Chlamydomonas*, there is a Y-shaped density (purple) that cradles the FAP52 density. The Y-shaped density is absent in *Tetrahymena*. In *Tetrahymena*, we observed Tether density 3, which is absent in *Chlamydomonas*.

Figure 2: 16-nm structure of *Chlamydomonas* doublet.

(A, B) 16-nm repeat structure of *Chlamydomonas* doublet and model at the IJ region. (C) Maps and model of PF A1 and B10, and IJ PF. The view is indicated in the schematic. Dashed boxes indicate the views in (D) and (E). Color scheme: α-tubulin: green; β-tubulin: blue; PACRG: gray; FAP20: dark gray; FAP276: purple. (D) Interaction of PACRG with the inter-dimer interface of tubulins from PF B10. (E) Electrostatic surface charge of PACRG, FAP20 and α- and β-tubulins of PF A1. Tubulin surface is negatively charged while the interacting interface of PACRG and FAP20 are positively charged. (F) The C-terminus of β-tubulin of PF A1 interacts with PACRG and FAP20. (G) Potential residues involved in the interaction of C-tail of β-tubulin and PACRG and FAP20. (H) The N-terminus of PACRG going into the wedge between PF A13 and A1. The N-terminus of *Chlamydomonas* PACRG (red color) forms a stable triple helix arrangement with the core of the protein. This is not observed in the human PACRG.

Figure 3: Structure of FAP52 and its interaction with tubulins and PACRG.

(A) Structure of FAP52 in a top view from the outside of the B-tubule looking down on the A-tubule. Black arrows indicate the direction of view in (B) and (H). (B, C) Interactions of FAP52 with α-tubulins from PF B8 and B9 and PACRG with (B) and without map overlay (C). (D-E) The structure of the α-K40 loop from PF B10. Red dashed boxes indicate the α-K40 loop. (F) Interaction of α-K40 loop of PF B9 and B10 with FAP52. In PF B10, residue D39 of α-tubulin appears to form a salt bridge with R225 from FAP52. In PF B9, T41 of α-tubulin appears to interact with segment G142-P143 from FAP52. (G) N275 from loop V268-L279 of FAP52 appears to interact with the N-terminus of PACRG in segment P25-A27. Loop V268-L279 in *Chlamydomonas* FAP52 is missing in the *Tetrahymena* and the human structures. (H-K)

Interactions of FAP276 with FAP52, FAP20 and tubulins. In (K) FAP52 model is digitally removed to show the interactions underneath.

Figure 4: Structure of the Tether densities.
(A) At higher resolution, Tether densities 1 and 2 appear to be a single polypeptide chain in both *Chlamydomonas* (A) and *Tetrahymena* (B). The dashed regions indicate the location of FAP52, which is digitally removed to show the Tether densities underneath. (C-D) The segmented Tether densities 1 and 2 from *Chlamydomonas* (C) and *Tetrahymena* (D). Most of the densities do not show a clear secondary structure pattern. Dashed boxes (E) and (G) show the helical regions of the Tether loop. (F) shows the proximal end of the Tether loop. (E) Tether density 1 consists of a clear coiled coil which inserts in the gap formed by four tubulin dimers, two from each of PF B9 and B10. (F) The end region of Tether density 2 is a loop that connects to the distal propeller of FAP52 and potentially interact with FAP276. (G) A small region in the middle of Tether densities 1 and 2 forms a helix that interacts with α-tubulin from PF A12. (H) Structure of Tether density 3 from *Tetrahymena*, which binds on top of the wedge between PF A13 and A1. (I) Overlay of the PACRG from *Chlamydomonas* onto the structure of *Tetrahymena* shows a hypothetical steric clash of a long *Tetrahymena* PACRG N-terminus with Tether density 3 (See also Fig. S4).

Figure 5: Proposed mechanism of IJ formation and B-tubule closure.
B-tubule starts growing laterally from the outer junction side as shown in (14). PACRG and FAP20 form a hetero-dimer, which binds onto the outside surface of PF A1. After this, multiple alternative hypotheses are possible. One hypothesis is that FAP52, FAP276 and the Tether density proteins would bind onto PF A12 and A13. FAP45 and other fMIP proteins would then be incorporated inside the B-tubule, which fixes the proper curvature so that PF B9 and B10 can interact with other IJ proteins. FAP52 binds both PF B9 and B10 through their K40 loops and finally, PACRG and FAP20 interact with the lateral side of PF B10 allowing B-tubule closure.

SUPPLEMENTARY MATERIALS

SUPPLEMENTARY FIGURE CAPTION

Figure S1: Data related to the doublet structures

(A) Schematics of fractionation of the axoneme in this study. Doublets were split from axoneme, and outside proteins were removed to obtain a simpler sample for cryo-EM. (B) A typical cryo-EM image of *Chlamydomonas* doublets. (C) Gold-standard Fourier Shell Correlation of the 48-nm repeat and 16-nm repeat doublet maps of *Chlamydomonas* and *Tetrahymena*. (D) Local resolution estimation of the 16-nm repeat maps from *Chlamydomonas* and *Tetrahymena* using MonoRes. The resolution of the B-tubule in *Tetrahymena* is lower due to the loss of the IJ PF. (E) The remaining PACRG- and FAP20-like densities in the *Tetrahymena* doublet structure. (F) Superimposition of the tomographic structure of the intact doublet (EMD-2132) with the 48-nm structure of the *Chlamydomonas* doublet in this study. The DRC is colored green. (G) Enlarged view of the missing PACRG unit at the IJ PF, where the DRC binds.

Figure S2: Atomic models of PACRG, FAP20, FAP52 and FAP276.

Atomic model of (A) PACRG, (C) FAP20, (E) FAP52 and (G) FAP276. Illustration of the cryo-EM density quality at selected regions of (B) PACRG, (D) FAP20, (F) FAP52 and (H) FAP276. (I) The atomic model of the IJ complex. Tubulins are removed for clarity. (J) PACRG and FAP20 form a heterodimer as indicated by brackets. (K, L) Electrostatic interactions between PACRG and FAP20 as illustrated by the surface charge. The dashed boxes in (J, K, L) highlight the interacting loops between PACRG and FAP20.

Figure S3: Data related to FAP52.

(A) Atomic model of *Chlamydomonas* FAP52 from inside the *Chlamydomonas* density map. (B) Atomic model of *Chlamydomonas* FAP52 fitted inside the *Tetrahymena* map highlights the longer loop (red) from *Chlamydomonas*. (C) Alignment of FAP52 from several species shows that *Chlamydomonas* has a longer loop in one beta propeller blade. The long loop is responsible for the interaction with PACRG. (D, E) α-K40 loop from PF B9 in *Chlamydomonas*. (F, G) Superimposition of the acetylated α-K40 loops from *Chlamydomonas* PF B9, B10 and *Tetrahymena* A12.

Figure S4: Data related to the Tether densities.

(A) Alternative view of the IJ region from *Chlamydomonas*. (B) Segmented hook density on top of A13. (C) Inter-PF angles of the A- and B-tubules from *Chlamydomonas* and *Tetrahymena* showing very similar angle distributions. (D) The N-terminus of PACRG and the hook density go into the wedges between PF A12 and A13, and PF A13 and A1, respectively. This likely contributes to the curvature of this region. (E) 90 degrees rotated view of (D). (F) The small

helix from *Tetrahymena* Tether loop appears to interact with α-tubulin, similar to *Chlamydomonas*.

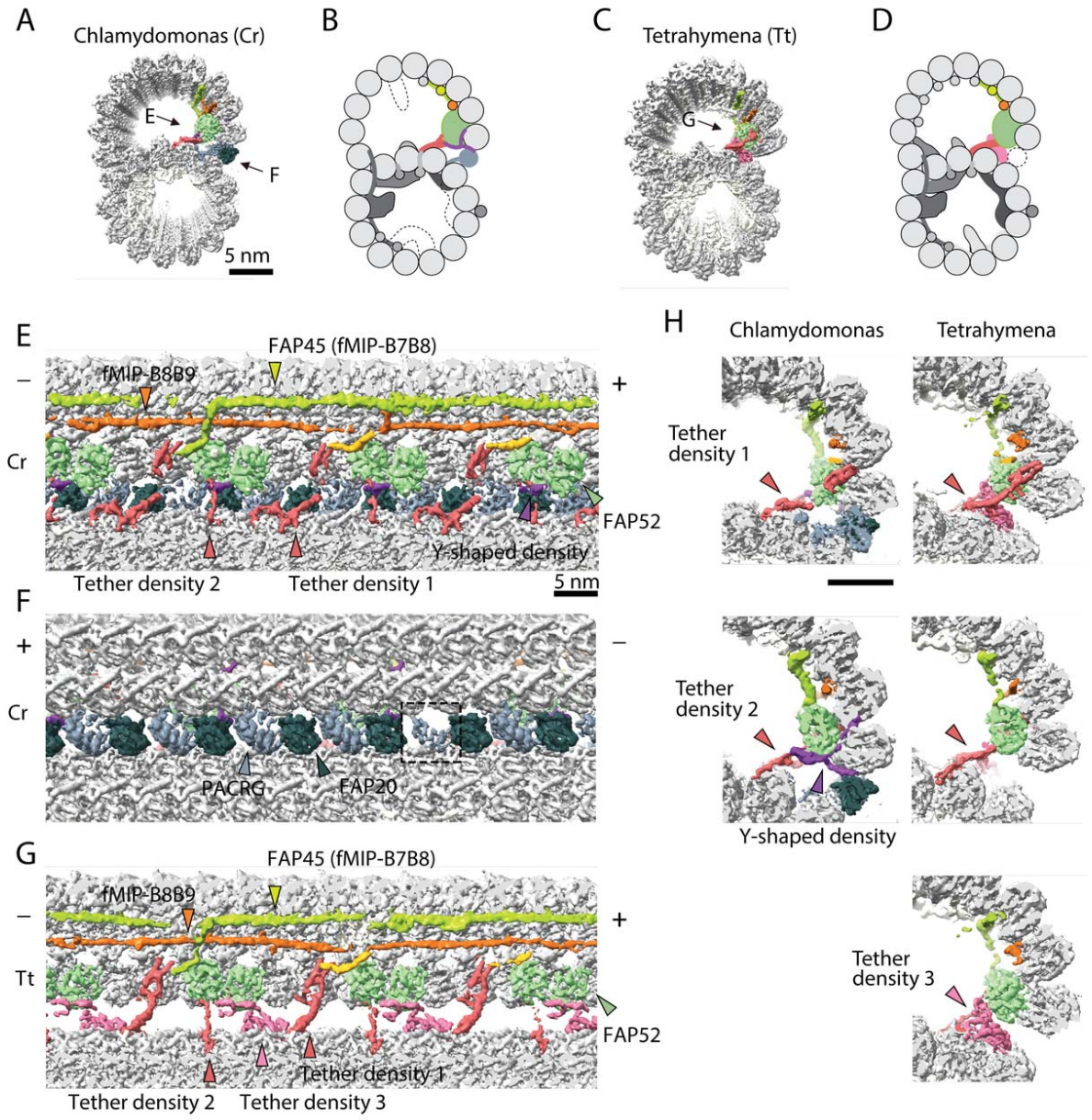

Fig. 1

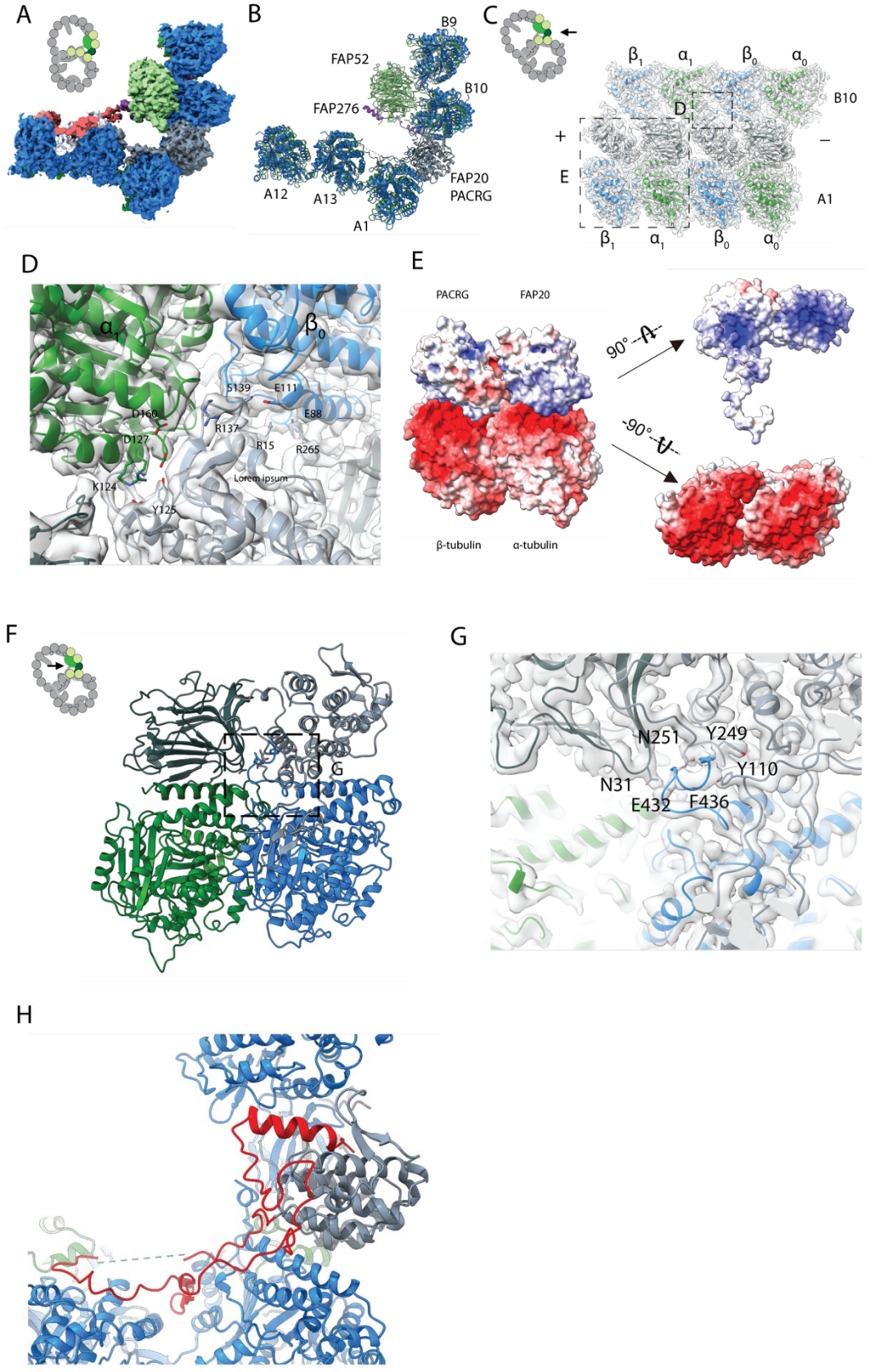

Figure 2

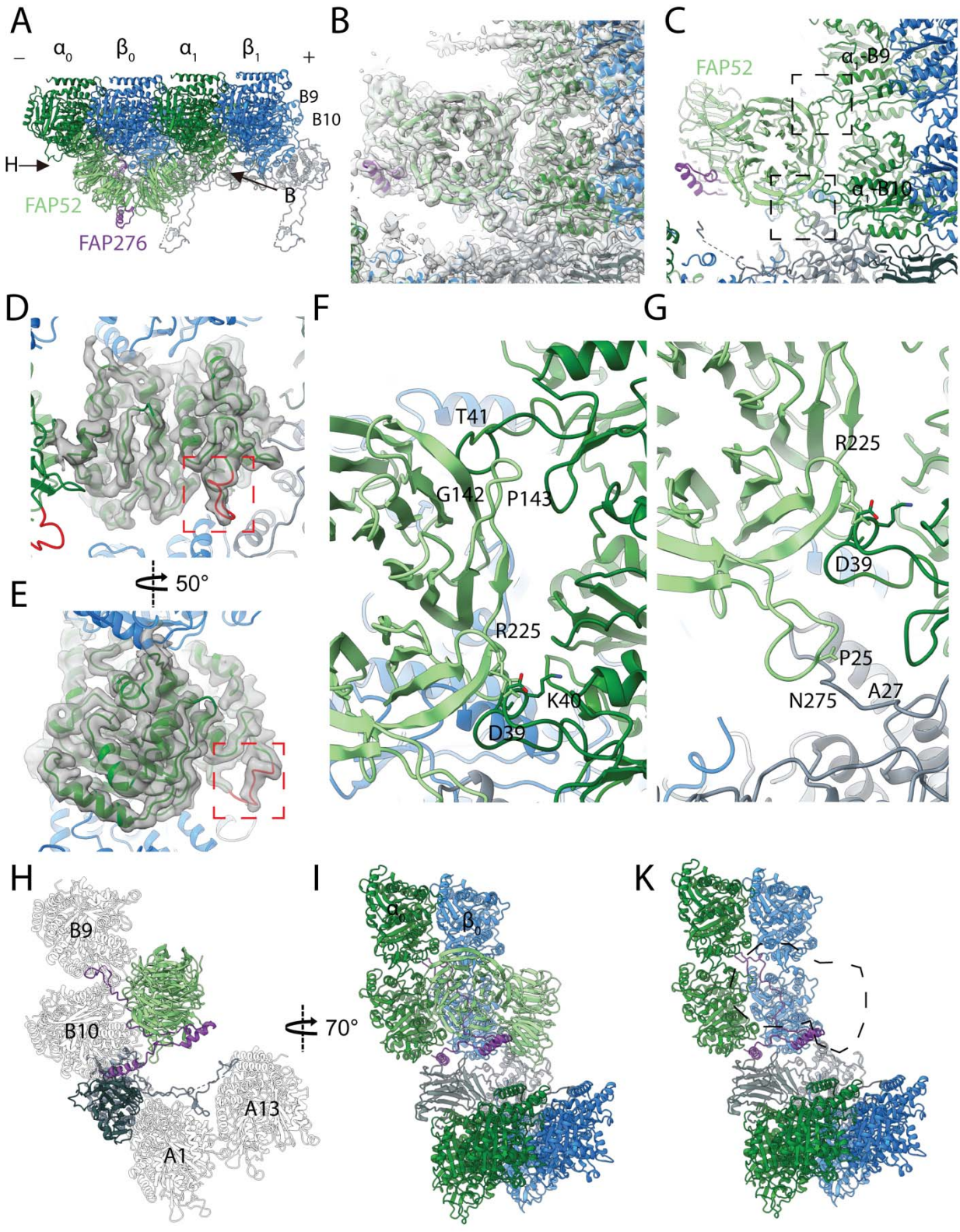

Figure 3

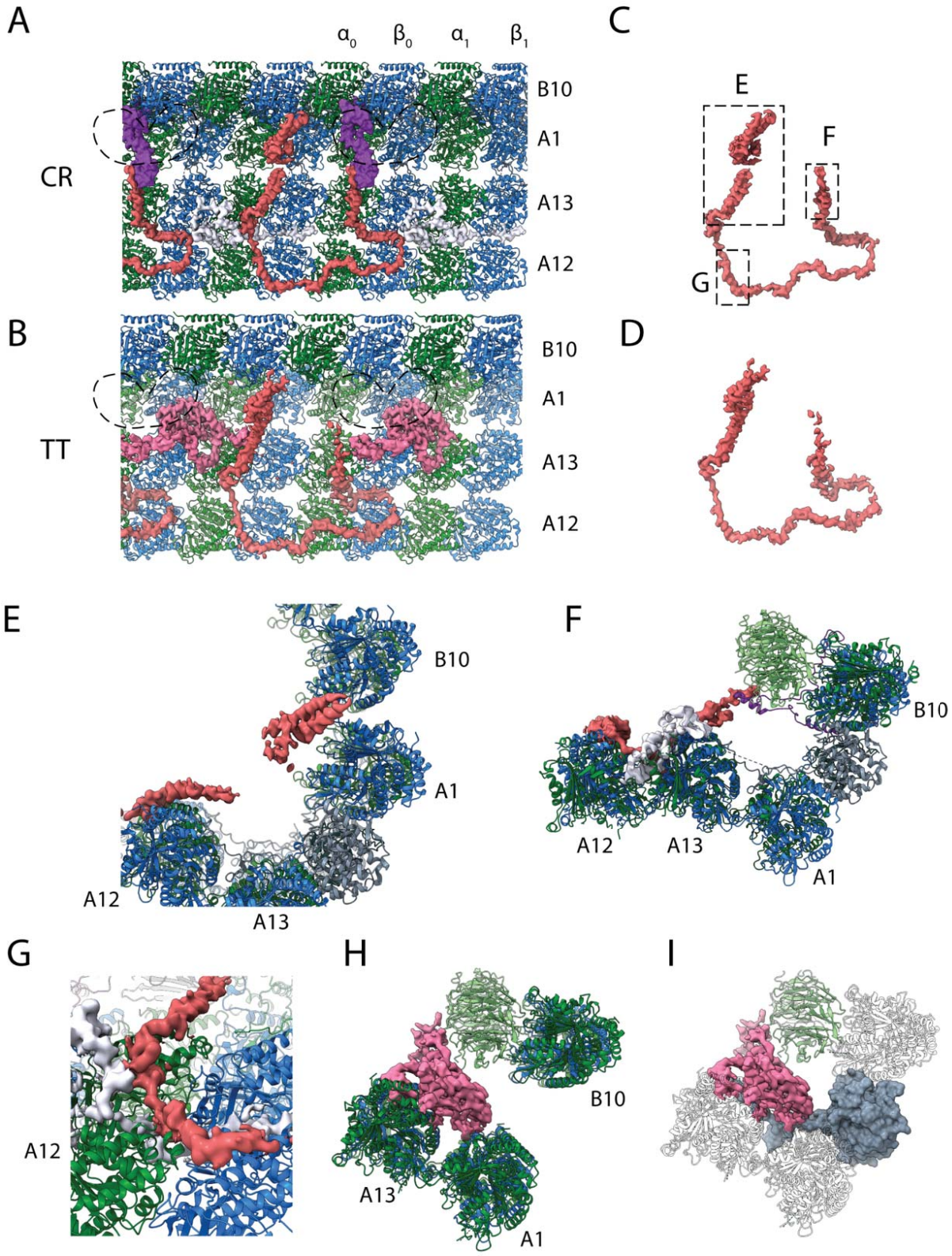

Figure 4

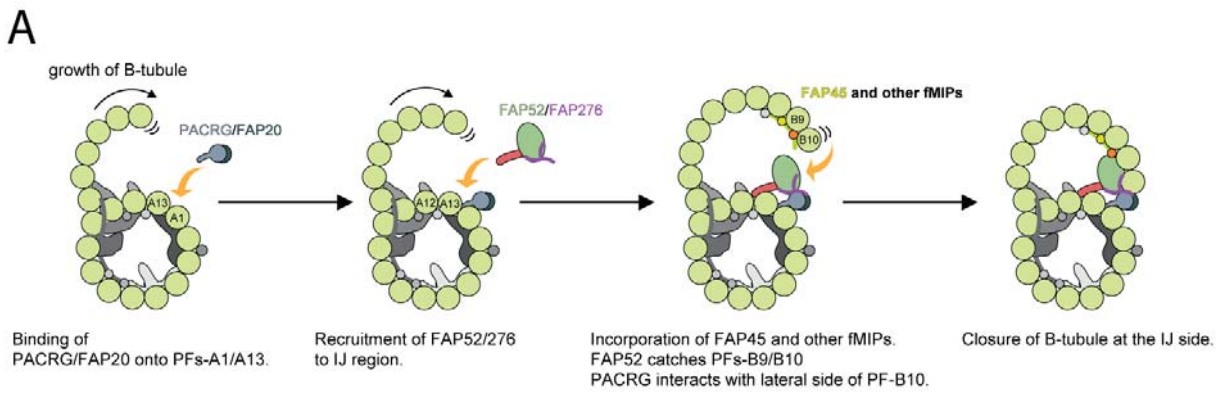

Figure 5.

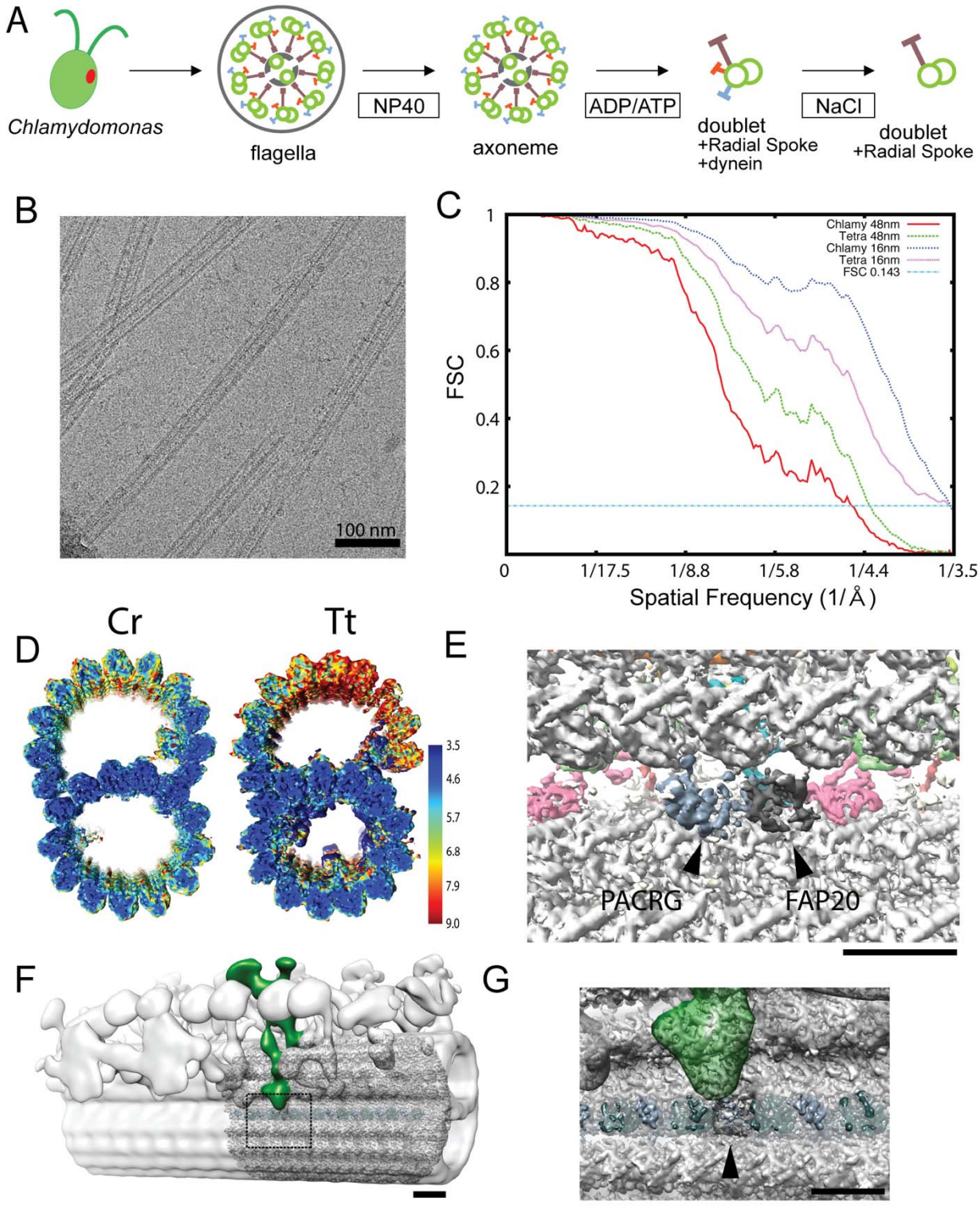

Figure S1

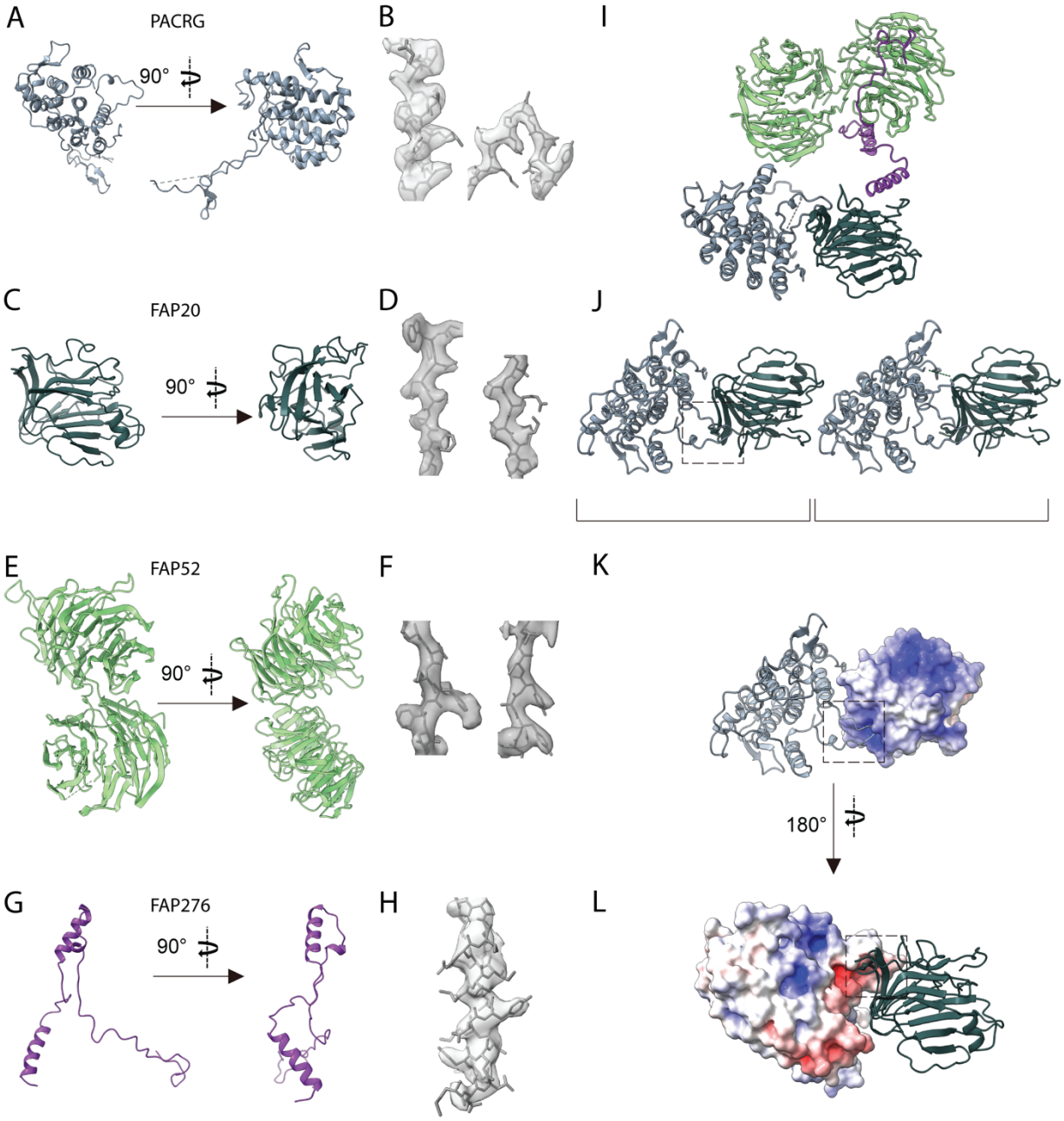

Figure S2

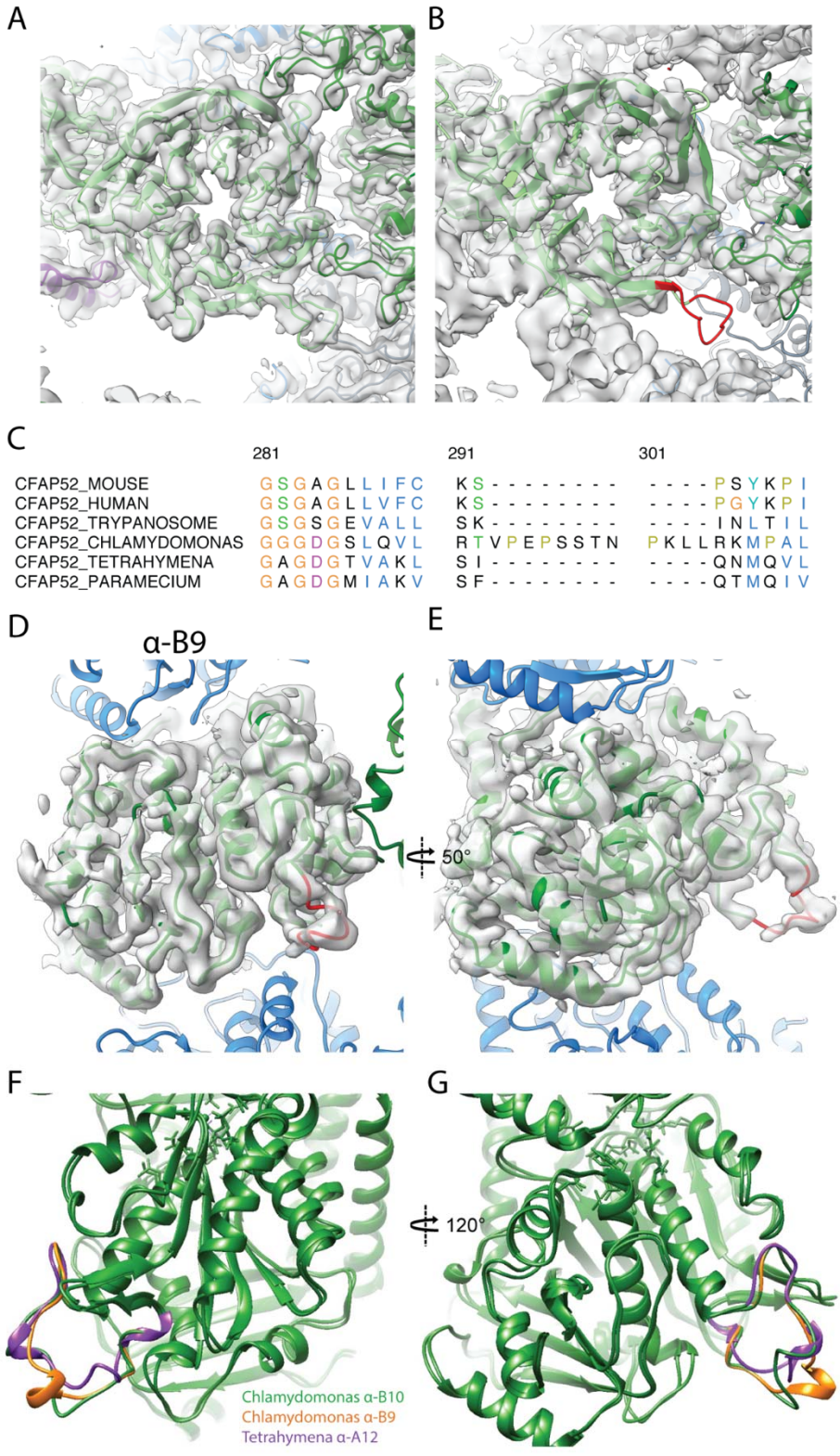

Figure S3

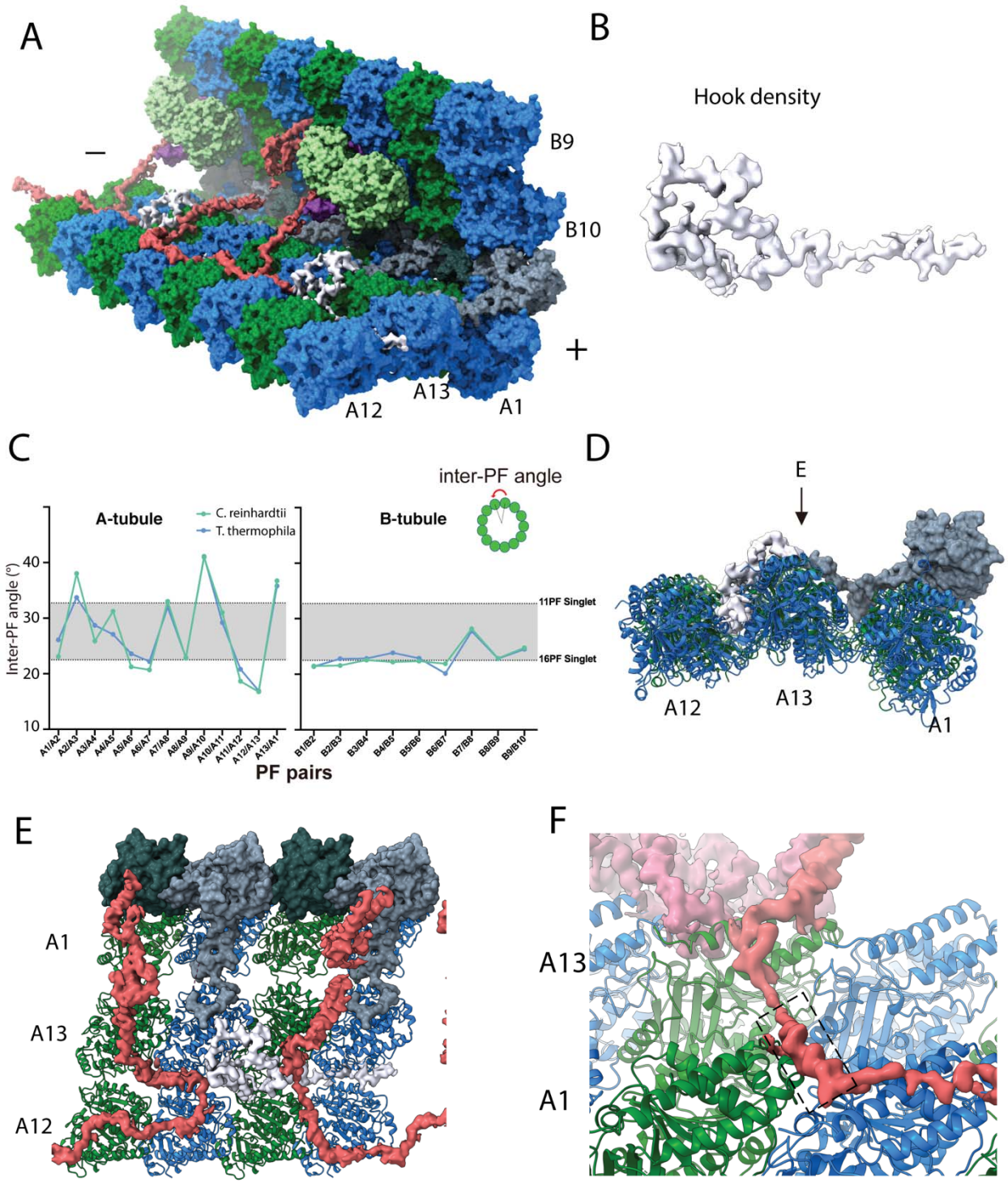

Figure S4

SUPPLEMENTARY TABLE

Supplementary Table 1: Significantly reduced or missing proteins in FAP52 compared to WT using relative mass spectrometry quantification.

Names	Uniprot ID	**WT** exclusive unique peptide counts (quantitative values after normalization)	**FAP52** exclusive unique peptide counts (quantitative values after normalization)	**FAP52/WT ratio** (quantitative values were used)	**p-values (WT vs FAP52)**	**Log2(Fold Change (FAP52/WT))**
FAP20	**A8IU92**	**14, 10, 12 (27, 19, 33)**	**14, 12, 13 (33, 17, 18)**	**0.86**	**0.65**	**-0.31**
FAP45	**A8I9E8**	**31, 27, 12 (60, 37, 33)**	**31, 30, 30 (48, 43, 40)**	**1.01**	**0.96**	**0.016**
PACRG	**A8I2Z6**	**13, 9, 10 (41, 26, 48)**	**15, 13, 13 (70, 42, 38)**	**1.30**	**0.38**	**0.38**
Tektin	**A8J8F6**	**20, 22, 14 (60, 61, 52)**	**29, 24 24 (74, 45, 43)**	**0.88**	**0.74**	**-0.096**
ARL3	A8ISN6	2, 2, 1 (2, 1, 2)	0, 0, 0 (0, 0, 0)	0.0	0.0013	-10.0
CHLREDRAFT_171815	A8HQQ4	2, 6, 1 (2, 5, 2)	0, 0, 0 (0, 0, 0)	0.0	0.035	-10.0
CHLREDRAFT_156073	A8I1U2	1, 1, 1 (2, 1, 2)	0, 0, 0 (0, 0, 0)	0.0	0.024	-10.0
FAP276	A8J9P2	3, 3, 2 (8 ,7, 14)	0, 0, 0 (0, 0, 0)	0.0	0.015	-10.0
CFAP52	A8ILK1	27, 21, 15 (59, 73, 105)	0, 0, 0 (0, 0, 0)	0.0	0.0046	-10.0
FAP36	A8IZX7	3, 3, 1 (3, 3, 2)	0, 0, 0 (0, 0, 0)	0.0	0.0023	-10.0
CrCDPK1	A8IHF4	3, 5, 2 (3, 4, 4)	0, 0, 0 (0, 0, 0)	0.0	<0.0001	-10.0
CHLREDRAFT_176830	A8J922	2, 1, 2 (2, 1, 1)	0, 0, 0 (0, 0, 0)	0.0	0.024	-10.0
FAP173	A8JAF7	3, 3, 1 (5, 3, 2)	0, 0, 0 (0, 0, 0)	0.0	0.012	-10.0
FAP29	A8J3X6	2, 3, 2 (3, 3, 4)	0, 0, 0 (0, 0, 0)	0.0	0.00045	-10.0
CHLREDRAFT_181390	A8JJY2	1, 1, 1 (1, 1, 2)	0, 0, 0 (0, 0, 0)	0.0	0.028	-10.0
ANK2	A8HNK2	1, 2, 1 (1, 1, 2)	0, 0, 0 (0, 0, 0)	0.0	0,0041	-10.0
FAP5	A8JAI0	11, 15, 7 (23, 22, 23)	2, 0, 0 (1, 0, 0)	0.014	<0.0001	-5.5
FAP164	A8JC79	4, 5, 1 (6, 4, 2)	0, 0, 1 (0, 0, 0)	0.0	0.022	-5.1
FAP288	A8IJV3	13, 12, 9 (18, 14, 23)	2, 1, 1 (1, 0, 0)	0.018	0.0021	-4.6

CHLREDRAFT_177061	A8J9A4	7, 7, 2 (8, 6, 4)	0, 1, 1 (0, 0, 0)	0.0	0.0071	-4.5
TEF20	A8IL00	2, 1, 1 (2, 1, 2)	0, 1, 0 (0, 0, 0)	0.0	0.036	-3.6
CHLREDRAFT_191579	A8J3S1	2, 4, 2 (3, 4, 4)	1, 0 ,1 (1, 0 , 0)	0.09	0.0003	-3.4
CHLREDRAFT_111330	A8IAY6	2, 2, 1 (3, 1, 2)	1, 0, 0 (1, 0, 0)	0.16	0.03	-3.2
14-3-3	Q7X7A7	9, 9, 3 (15, 10, 6)	5, 0, 1 (4, 0, 0)	0.13	0.03	-3.0
Isocitrate lyase	A8J244	12, 8, 9 (23, 8, 19)	6, 2, 2 (5, 1, 1)	0.14	0.036	-2.9
CHLREDRAFT_141580	A8I9N1	7, 11, 4 (13, 16, 17)	3, 3, 3 (3, 2, 2)	0.19	0.0006	-2.7
Elongation Factor 2	A8JHX9	15,17,5 (27, 22, 10)	3, 6, 6 (3, 3, 3)	0.15	0.026	-2.7
CHLREDRAFT_189452	A8IT59	4, 6, 1 (5, 5, 2)	1, 1, 1 (1, 0, 1)	0.17	0.026	-2.7
CHLREDRAFT_175290	A8J364	4, 3, 2 (5, 3, 6)	1, 2, 2 (1, 1, 1)	0.21	0.014	-2.6
CHLREDRAFT_111269	A8IBY2	1, 4, 1 (1, 3, 2)	0, 2, 1 (0, 1, 0)	0.17	0.045	-2.4
FAP138	A8IUQ2	4, 6, 3 (8, 7, 6)	2, 3, 3 (1, 1, 1)	0.14	0.00046	-2.4
FAP31	A8JDM7	6, 8, 4 (8, 7, 8)	7, 0, 0 (5, 0, 0)	0.21	0.024	-2.2
IFT80	A8IXE2	4, 5, 1 (5, 4, 2)	1, 1, 2 (1, 1, 1)	0.27	0.022	-2.2
CHLREDRAFT_189792	A8HPX1	16, 21, 6 (18, 17, 12)	0, 11, 13 (0, 6, 5)	0.23	0.0096	-2.1
CHLREDRAFT_206178	A8IP72	17, 24, 10 (20, 19,23)	0, 15, 18 (0, 7, 8)	0.24	0.0053	-2.0
GSK3	Q6IV67	4, 3, 2 (5, 2, 4)	2, 2, 1 (1, 1, 0)	0.18	0.030	-1.8
CHLREDRAFT_144025	A8IF86	13, 27, 14 (16, 27, 35)	14, 12, 13 (11, 7, 7)	0.32	0.035	-1.7
FAP148	A8IAT9	29, 41, 11 (44, 52, 27)	14, 22, 26 (14, 12, 15)	0.33	0.022	-1.6
FAP85	A8J250	7, 11, 6 (14, 15, 19)	8, 4, 4 (10, 3, 2)	0.31	0.024	-1.6
Phototropin	A8IXU7	30, 22, 18 (56, 44, 64)	25, 14, 17 (41,12, 13)	0.40	0.041	-1.3
p38	A4PET3	3, 8, 4 (7 ,7, 8)	5, 3, 3 (5, 2, 1)	0.36	0.019	-1.3
FAP39	A8J0V2	6, 10, 4 (13, 11, 8)	9, 5, 4 (7, 4, 3)	0.42	0.022	-1.1

REFERENCES

1. P. Satir, S. T. Christensen, Overview of structure and function of mammalian cilia. *Annual review of physiology* **69**, 377-400 (2007).
2. T. W. Hurd, F. Hildebrandt, Mechanisms of nephronophthisis and related ciliopathies. *Nephron Exp Nephrol* **118**, e9-14 (2011).
3. K. H. Bui, H. Sakakibara, T. Movassagh, K. Oiwa, T. Ishikawa, Molecular architecture of inner dynein arms in situ in Chlamydomonas reinhardtii flagella. *The Journal of cell biology* **183**, 923-932 (2008).
4. K. H. Bui, H. Sakakibara, T. Movassagh, K. Oiwa, T. Ishikawa, Asymmetry of inner dynein arms and inter-doublet links in Chlamydomonas flagella. *The Journal of cell biology* **186**, 437-446 (2009).
5. K. H. Bui, T. Yagi, R. Yamamoto, R. Kamiya, T. Ishikawa, Polarity and asymmetry in the arrangement of dynein and related structures in the Chlamydomonas axoneme. *The Journal of cell biology* **198**, 913-925 (2012).
6. T. Heuser, M. Raytchev, J. Krell, M. E. Porter, D. Nicastro, The dynein regulatory complex is the nexin link and a major regulatory node in cilia and flagella. *The Journal of cell biology* **187**, 921-933 (2009).
7. M. Ichikawa *et al.*, Subnanometre-resolution structure of the doublet microtubule reveals new classes of microtubule-associated proteins. *Nature communications* **8**, 15035 (2017).
8. M. Ichikawa *et al.*, Tubulin lattice in cilia is in a stressed form regulated by microtubule inner proteins. *Proceedings of the National Academy of Sciences* (2019).
9. L. G. Tilney *et al.*, Microtubules: evidence for 13 protofilaments. *The Journal of cell biology* **59**, 267-275 (1973).
10. R. W. Linck, R. E. Stephens, Functional protofilament numbering of ciliary, flagellar, and centriolar microtubules. *Cell Motil Cytoskeleton* **64**, 489-495 (2007).
11. D. Nicastro *et al.*, Cryo-electron tomography reveals conserved features of doublet microtubules in flagella. *Proceedings of the National Academy of Sciences of the United States of America* **108**, E845-853 (2011).
12. S. Sun, R. L. Fisher, S. S. Bowser, B. T. Pentecost, H. Sui, Three-dimensional architecture of epithelial primary cilia. *Proceedings of the National Academy of Sciences of the United States of America* **116**, 9370-9379 (2019).
13. U. Euteneuer, J. R. McIntosh, Polarity of midbody and phragmoplast microtubules. *The Journal of cell biology* **87**, 509-515 (1980).
14. M. Schmidt-Cernohorska *et al.*, Flagellar microtubule doublet assembly in vitro reveals a regulatory role of tubulin C-terminal tails. *Science* **363**, 285-288 (2019).
15. H. A. Yanagisawa *et al.*, FAP20 is an inner junction protein of doublet microtubules essential for both the planar asymmetrical waveform and stability of flagella in Chlamydomonas. *Molecular biology of the cell* **25**, 1472-1483 (2014).
16. E. E. Dymek *et al.*, PACRG and FAP20 form the inner junction of axonemal doublet microtubules and regulate ciliary motility. *Molecular biology of the cell* **30**, 1805-1816 (2019).
17. T. Kitada *et al.*, Mutations in the parkin gene cause autosomal recessive juvenile parkinsonism. *Nature* **392**, 605-608 (1998).
18. A. B. West, P. J. Lockhart, C. O'Farell, M. J. Farrer, Identification of a novel gene linked to parkin via a bi-directional promoter. *Journal of molecular biology* **326**, 11-19 (2003).
19. T. Thumberger *et al.*, Ciliary and non-ciliary expression and function of PACRG during vertebrate development. *Cilia* **1**, 13 (2012).

20. D. Lorenzetti, C. E. Bishop, M. J. Justice, Deletion of the Parkin coregulated gene causes male sterility in the quaking(viable) mouse mutant. *Proceedings of the National Academy of Sciences of the United States of America* **101**, 8402-8407 (2004).
21. G. R. Wilson *et al.*, Deletion of the Parkin co-regulated gene causes defects in ependymal ciliary motility and hydrocephalus in the quakingviable mutant mouse. *Hum Mol Genet* **19**, 1593-1602 (2010).
22. C. Laligne *et al.*, Bug22p, a conserved centrosomal/ciliary protein also present in higher plants, is required for an effective ciliary stroke in Paramecium. *Eukaryot Cell* **9**, 645-655 (2010).
23. M. Owa *et al.*, Inner lumen proteins stabilize doublet microtubules in cilia and flagella. *Nature communications* **10**, 1143 (2019).
24. A. Ta-Shma *et al.*, A human laterality disorder associated with a homozygous WDR16 deletion. *Eur J Hum Genet* **23**, 1262-1265 (2015).
25. G. J. Brouhard *et al.*, XMAP215 is a processive microtubule polymerase. *Cell* **132**, 79-88 (2008).
26. J. B. Leano, K. C. Slep, Structures of TOG1 and TOG2 from the human microtubule dynamics regulator CLASP1. *PLoS One* **14**, e0219823 (2019).
27. N. L. Dawson *et al.*, CATH: an expanded resource to predict protein function through structure and sequence. *Nucleic Acids Res* **45**, D289-D295 (2017).
28. D. Wloga, E. Joachimiak, P. Louka, J. Gaertig, Posttranslational Modifications of Tubulin and Cilia. *Cold Spring Harb Perspect Biol* **9** (2017).
29. L. Eshun-Wilson *et al.*, Effects of alpha-tubulin acetylation on microtubule structure and stability. *Proceedings of the National Academy of Sciences of the United States of America* **116**, 10366-10371 (2019).
30. E. H. Kellogg *et al.*, Near-atomic model of microtubule-tau interactions. *Science* **360**, 1242-1246 (2018).
31. N. Khan *et al.*, Crystal structure of human PACRG in complex with MEIG1. *BioRvix* (2019).
32. C. Herve *et al.*, Carbohydrate-binding modules promote the enzymatic deconstruction of intact plant cell walls by targeting and proximity effects. *Proceedings of the National Academy of Sciences of the United States of America* **107**, 15293-15298 (2010).
33. S. Bechstedt, G. J. Brouhard, Doublecortin recognizes the 13-protofilament microtubule cooperatively and tracks microtubule ends. *Dev Cell* **23**, 181-192 (2012).
34. M. LeDizet, G. Piperno, Identification of an acetylation site of Chlamydomonas alpha-tubulin. *Proceedings of the National Academy of Sciences of the United States of America* **84**, 5720-5724 (1987).
35. D. R. Friedmann, A. Aguilar, J. Fan, M. V. Nachury, R. Marmorstein, Structure of the alpha-tubulin acetyltransferase, alphaTAT1, and implications for tubulin-specific acetylation. *Proceedings of the National Academy of Sciences of the United States of America* **109**, 19655-19660 (2012).
36. D. Portran, L. Schaedel, Z. Xu, M. Thery, M. V. Nachury, Tubulin acetylation protects long-lived microtubules against mechanical ageing. *Nat Cell Biol* **19**, 391-398 (2017).
37. Z. Xu *et al.*, Microtubules acquire resistance from mechanical breakage through intralumenal acetylation. *Science* **356**, 328-332 (2017).
38. N. Kalebic *et al.*, alphaTAT1 is the major alpha-tubulin acetyltransferase in mice. *Nature communications* **4**, 1962 (2013).
39. J. D. Alper, F. Decker, B. Agana, J. Howard, The motility of axonemal dynein is regulated by the tubulin code. *Biophys J* **107**, 2872-2880 (2014).
40. P. R. Burton, Luminal material in microtubules of frog olfactory axons: structure and distribution. *The Journal of cell biology* **99**, 520-528 (1984).

41. K. F. Lechtreck, S. Geimer, Distribution of polyglutamylated tubulin in the flagellar apparatus of green flagellates. *Cell Motil Cytoskeleton* **47**, 219-235 (2000).
42. N. Pathak, T. Obara, S. Mangos, Y. Liu, I. A. Drummond, The zebrafish fleer gene encodes an essential regulator of cilia tubulin polyglutamylation. *Molecular biology of the cell* **18**, 4353-4364 (2007).
43. G. B. Witman, Isolation of Chlamydomonas flagella and flagellar axonemes. *Methods in enzymology* **134**, 280-290 (1986).
44. S. Q. Zheng *et al.*, MotionCor2: anisotropic correction of beam-induced motion for improved cryo-electron microscopy. *Nature methods* **14**, 331-332 (2017).
45. K. Zhang, Gctf: Real-time CTF determination and correction. *Journal of structural biology* **193**, 1-12 (2016).
46. G. Tang *et al.*, EMAN2: an extensible image processing suite for electron microscopy. *Journal of structural biology* **157**, 38-46 (2007).
47. J. Zivanov *et al.*, New tools for automated high-resolution cryo-EM structure determination in RELION-3. *Elife* **7** (2018).
48. J. L. Vilas *et al.*, MonoRes: Automatic and Accurate Estimation of Local Resolution for Electron Microscopy Maps. *Structure* **26**, 337-344 e334 (2018).
49. B. Webb, A. Sali, Protein structure modeling with MODELLER. *Methods Mol Biol* **1137**, 1-15 (2014).
50. P. V. Afonine *et al.*, Real-space refinement in PHENIX for cryo-EM and crystallography. *Acta Crystallogr D Struct Biol* **74**, 531-544 (2018).
51. P. D. Adams *et al.*, PHENIX: a comprehensive Python-based system for macromolecular structure solution. *Acta Crystallogr D Biol Crystallogr* **66**, 213-221 (2010).
52. P. Emsley, B. Lohkamp, W. G. Scott, K. Cowtan, Features and development of Coot. *Acta Crystallogr D Biol Crystallogr* **66**, 486-501 (2010).
53. J. Yang *et al.*, The I-TASSER Suite: protein structure and function prediction. *Nature methods* **12**, 7-8 (2015).
54. A. Drozdetskiy, C. Cole, J. Procter, G. J. Barton, JPred4: a protein secondary structure prediction server. *Nucleic Acids Res* **43**, W389-394 (2015).
55. E. F. Pettersen *et al.*, UCSF Chimera--a visualization system for exploratory research and analysis. *J Comput Chem* **25**, 1605-1612 (2004).
56. T. D. Goddard *et al.*, UCSF ChimeraX: Meeting modern challenges in visualization and analysis. *Protein Sci* **27**, 14-25 (2018).
57. D. Dai, M. Ichikawa, K. Peri, R. Rebinsky, K. H. Bui, Identification and mapping of central pair proteins by proteomic analysis. *bioRxiv* (2019).